Supporting Information

Logic-OR gate gold nanorods-based plasmonic biosensor for multipathogen detection and photothermal disinfection

Francesca Petronella*[a], Daniela De Biase [b], Carlo Santini [c], Arianna Avitabile [b], Maria Laura Sforza [b], Federica Zaccagnini [b], Antonio d'Alessandro [c], Luciano De Sio*[b]

[a].   National Research Council of Italy, Institute of Crystallography CNR-IC, Montelibretti Division Area territoriale di Ricerca di Roma 1 Strada Provinciale 35d, n. 9 – 00010 Montelibretti (RM)

[b].   Department of Medico-Surgical Sciences and Biotechnologies, Sapienza University of Rome, Corso della Repubblica 79, 04100 Latina, Italy

[c].   Department of Information Engineering, Electronics and Telecommunications, Sapienza University of Rome, Via Eudossiana n° 18, 00184 Rome, Italy
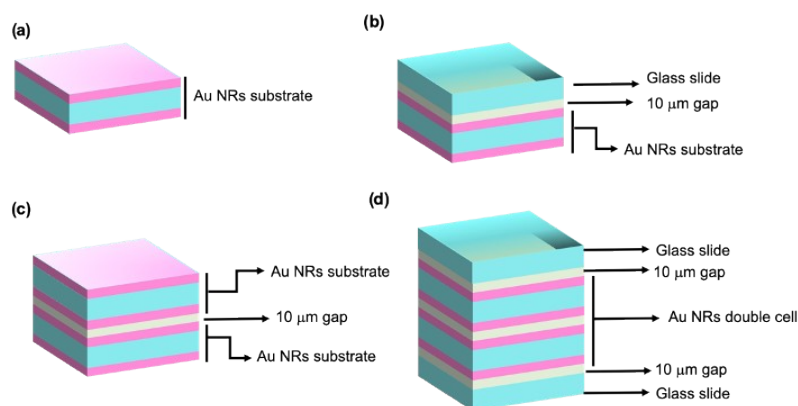

Figure SI 1 Schematic representation of the AuNR array. The pink surfaces indicate the presence of the AuNR array. The AuNRs are immobilized on both sides of the glass substrate **(a).** Single cell prepared by using one AuNR array **(b)**. Plasmonic cascade AuNR array resulting from assembling two AuNR arrays **(c).** Cascade AuNR array CG obtained by covering with two glass slides (at the top and bottom) the cascade AuNR array **(d).**

SI 1: Schematic representation of a cascade AuNRs array

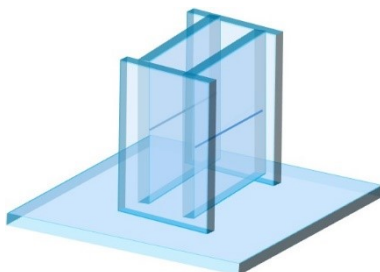## SI 2: Schematic representation of the functionalization chamber

Figure SI 2 Functionalization chamber realized to bioactivate the AuNR array with two different monoclonal antibodies in two distinct areas of the array.

SI 3: Spectroscopic measurements of AuNRs/AbE/AbS samples
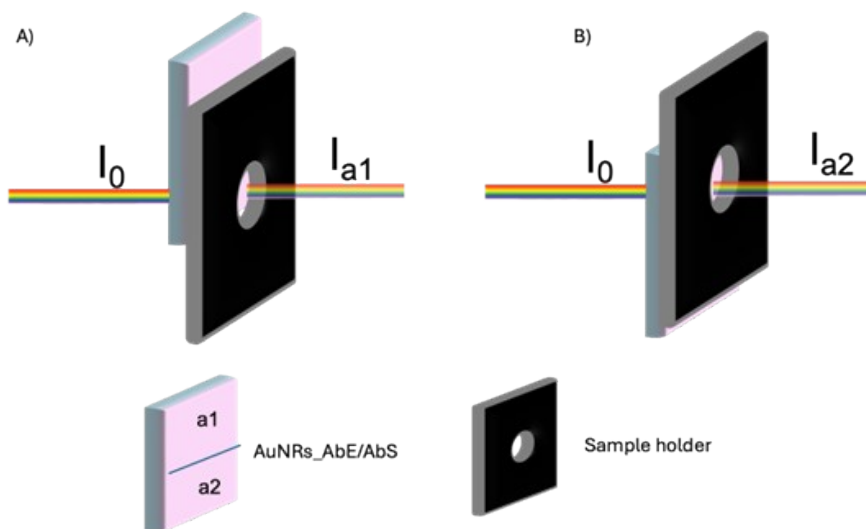

Figure SI 3 Schematic illustrating how the AuNRs/AbE/AbS samples are positioned in the spectrophotometer's sample holder, enabling selective measurement of the absorption spectrum in areas a1 or a2, respectively.

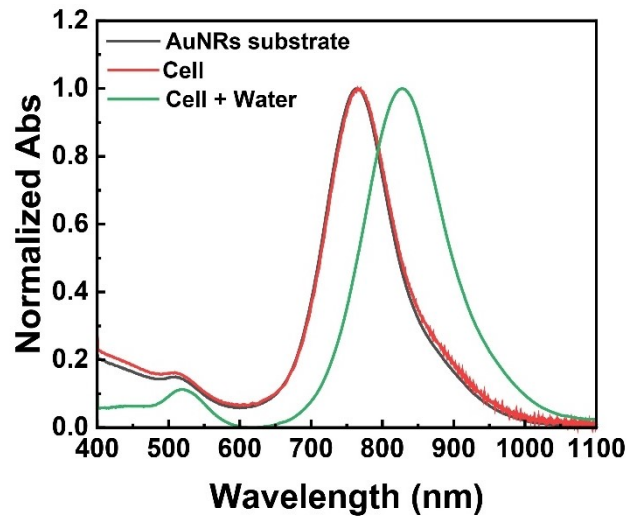## SI 4: Sensitivity to the refractive index change

Figure SI 4 Absorption spectrum of an AuNRs array (black line) and AuNRs single cell before (red line) and after (green line) infiltration with water. The red shift points out the sensitivity to n change.

The AuNR array developed in the present work were designed to provide a spectroscopic response as a function of the refractive index (*n*) of the surrounding medium. In particular, the LPB wavelength's optical shift, induced by *n* changes, was selected as a suitable sensing parameter. Indeed, the LPB shift is more sensitive to *n* alterations to the one of the transverse plasmon band (TPB).[1] The AuNRs arrays were used to fabricate cells, with a gap that capillary forces can fill with the desired chemical compound. In the actual case, the gap of the cells was infiltrated with water.[2] **Figure SI 4** illustrates the spectral response of the AuNRs cell before (red line) and after (green line) the infiltration with water. The black track of **Figure SI 4** shows the spectrum of the respective AuNRs substrate for comparison. The AuNRs substrate shows its LPB centered at 765 nm. No significant optical shift was measured when the AuNRs array was utilized to fabricate the cell. The FWHM remained almost unaltered, from 112 nm for the AuNRs array to 113 nm for the AuNRs glass cell. After infiltrating the cell with water, the LPB red-shifted by 62.5 nm, from 765 nm to 827.5 nm, and broadened the peak, yielding an FWHM of 133 nm.

SI 5: Statistical analysis using SEM micrographs

The values of the AuNRs length, interparticle distance, and horizontal and vertical angle were obtained from analyzing 50 objects for each micrograph (i.e., Figures 1e).

SI 5.1 AuNRs length

The chi-square test was performed analysing the histogram in **Figure SI 5a**, which reports the statistical distribution of the AuNRs length measured by considering 50 AuNRs. It resulted in ~ 1.504 with 7 degrees of freedom, corresponding to:

$$P_7(c^2 \geq c_0^2) = 16\%$$ (equation SI 1)

Despite its low probability percentage, the distribution can still be considered Gaussian.

SI 5.2 AuNRs interparticle distance

The chi-square test was performed analysing the histogram in **Figure SI 5b,** which reports the statistical distribution of the AuNRs interparticle distance measured by considering 50 AuNRs. The chi-square test yielded a reduced chi-square value of ~ 0.699 with eight degrees of freedom, corresponding to:

$$P_8(c^2 \geq c_0^2) = 70\%$$ (equation SI 2)

With a statistical acceptance threshold of 5%, it can be concluded that the distribution of distances is expected around the mean.

SI 5.3 Statistic analysis on the orientation (angular distribution) of AuNRs immobilized on the glass substrate

The orientation of AuNRs immobilized on the glass substrate was evaluated by measuring the angle formed by a selected AuNR and the horizontal and vertical axes, resulting in the horizontal and vertical angles, respectively. The statistical distribution of the horizontal and vertical angles, obtained by considering 50 objects, is reported in the histograms in Figure **SI 5c** and **SI 5d.**

The two histograms were used to carry out the two respective chi-square tests, assuming a uniform angle distribution due to the expected random arrangement of AuNRs. The reduced chi-square value for the horizontal angle was ~ 0.416 with 5 degrees of freedom, corresponding to:

$$P_5(c^2 \geq c_0^2) = 85\% \qquad \text{(equation SI 3)}$$

Therefore, the orientation of particles calculated to the horizontal axis can be considered random. The reduced chi-square value for the vertical angle was ~ 0.416, with five degrees of freedom, corresponding to:

$$P_5(c^2 \geq c_0^2) = 42\% \qquad \text{(equation SI 4)}$$

Therefore, the orientation of particles calculated to the vertical axis can also be considered random. Finally, the order parameter was considered. It was calculated using the equation:

$$S = \langle P_2(cos\theta) \rangle = \left| \frac{3cos^2\theta - 1}{2} \right|, \ S \in [0,1] \qquad \text{(equation SI 5)}$$

The order parameters obtained, considering the horizontal and vertical angles, are reported in **Table SI 1.**
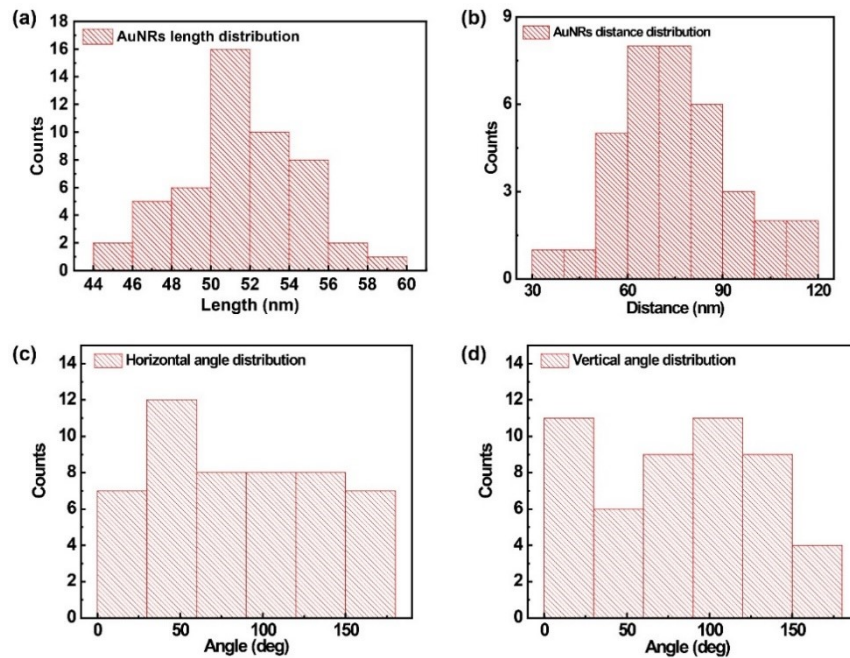

Figure SI 5 Statistical characterization of samples. AuNRs length distribution. **(a).** AuNRs interparticle distance distribution. **(b)**. AuNRs angular distribution with angle measured to the horizontal axis **(c).** AuNRs angular distribution with angle measured to the vertical axis **(d).**

Table SI 1: Summary of values derived from statistical analysis of SEM micrographs of AuNRs substrates.

PARAMETER	NUMERICAL VALUE
AUNRS LENGHT	*51,5 nm ± 3,0 nm*
INTERPARTICLE DISTANCE	*75,4 nm ± 18,8 nm*
HORIZONTAL ANGLE	*84,9 °*
VERTICAL ANGLE	*80,3°*
HORIZONTAL ORDER PARAMETER	*0,28*
VERTICAL ORDER PARAMETER	*0,17*

SI 6: Photothermal properties of the AuNR array under NIR laser irradiation
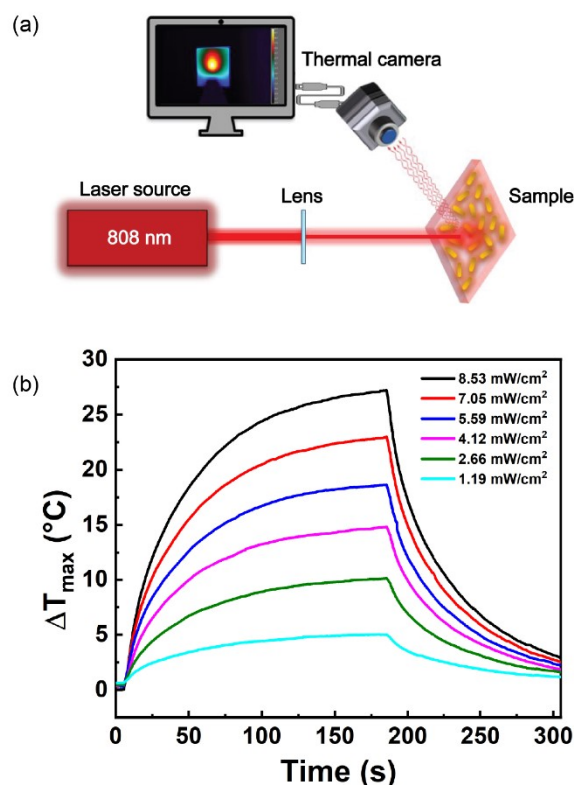

Figure SI 6 Schematic of thermo-optical setup used for the PT characterization of the AuNRs array under NIR laser irradiation (a). PT characterization of the AuNR array under NIR laser irradiation. Time-temperature increase profiles as a function of irradiation time were measured at different values of laser intensity, considering the maximum temperature values T_{max} (b).

Leveraging AuNRs' extraordinary ability to generate heating due to their PT properties, we investigated the PT properties of AuNR arrays. The PT characterization was performed using the thermo-optical setup reported in **Figure SI 6a**, equipped with an 808 nm NIR laser.

Figure SI 6b shows the maximum temperature variation (ΔT) (calculated to room temperature) as a function of the irradiation time.

The time-ΔT_{max} profiles were obtained at different laser intensities ranging from 1.19 W/cm^2 to 8.53 W/cm^2. Experimental data highlight the increase in ΔT_{max} values as the laser intensity increases, reaching a ΔT_{max} of 54.7 °C when the intensity was set at 8.53 W/cm^2. The PT behaviour reported in **Figure SI 6b** is consistent with theoretical investigations and previously reported measurements performed in colloidal dispersions and on substrates.

SI 7: Numerical simulations

Numerical simulations were performed by considering an elemental unit of 30 AuNRs randomly distributed on 0.25 µm² of an air-surmounted glass domain to represent a limited portion of the AuNR array. Moreover, an average density of 120 AuNRs/µm² positioned in the focal spot of the illuminating laser was considered. **Figure SI 7a** shows the elemental simulation domain, consisting of a glass substrate (*n* glass=1.33), whose upper surface is functionalized by 30 randomly oriented AuNRs, surmounted by an air cladding (*n* air=1). The simulation domain's length, width, and height are 500 nm, 500 nm, and 800 nm, respectively.
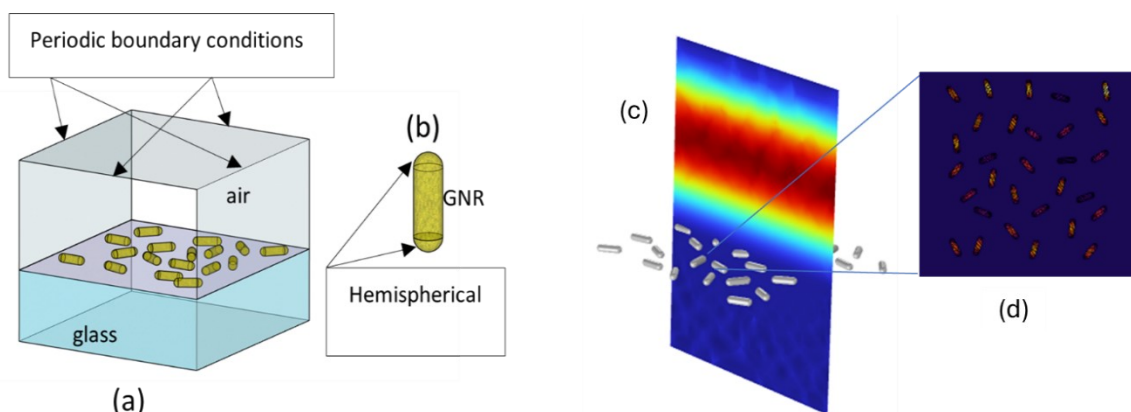

Figure SI 7 Graphical representation of the FEM simulation element. A plane EM wave orthogonally impinging from the air cladding on AuNRs deposited on a glass substrate. The solution of the EM field involves the position of periodic conditions on side boundaries and the definition of a Perfectly Matched Layer enclosing the simulation domain, whose length, width, and height are 500 nm, 500 nm, and 800 nm, respectively. **(a)** Magnification of a cylindrical AuNR with hemispherical caps. Average dimensions of AuNRs are 51.5 nm in length and 15 nm in diameter **(b)**. COMSOL modeling of the 30 random AuNRs. Norm of the incident Electric field **(c)**. Magnification showing power loss density in AuNRs **(d)**.

An electromagnetic (EM) plane-wave, linearly polarized, having λ= 808 nm, representing the paraxial portion of the illuminating laser beam, is excited at the upper boundary of the air cladding and is orthogonally incident to the plane surface of the AuNR array. The presence of the larger structure

and relevant laser excitation is taken into account by suitably imposing periodic Flouquet boundary conditions on the side boundaries of the simulation domain and by enclosing the simulation cell in an EM perfectly matched layer.

AuNRs are modeled as hemispherical-capped AuNRs, whose mean value and standard deviation of length lGNR = (51±3) nm and diameter dGNR= (15±0.9) nm consistent with the results of the geometrical characterization performed on SEM images (**Figures 1e** and **1f** and **Figure SI 5**) of experimental samples. A magnification of the AuNRs structure is represented as inset **(b)** of **Figure SI 7a**. The EM behavior of Au in the wavelength region under analysis is modelled using a wavelength-dependent complex permittivity, whose values for real and imaginary parts are deduced by interpolation from experimental data available in the literature[.3]

Starting from the evaluation of incident EM fields, reflected and refracted by the planar glass surface, acting as a background solution for the numerical solver, the assessment of the AuNRs-scattered field leads to the evaluation of the total EM field, allowing the numerical estimation of power-loss density qe in the NPs' volume, defined as:

$$q_e(\omega,r) = \frac{1}{2}\omega\varepsilon_0 Im[\epsilon_A u(\omega)]|E(r)|^2$$

(equation SI 6)

where ω is the angular frequency of the incident radiation. An image showing a plot of the norm of the electric field incident on the AuNRs and a power-loss density qe in the AuNRs volume is shown in **Figure SI 7c**.

By integrating qe in the whole AuNRs' volume, the total power absorbed by the AuNRs Qe is evaluated as:

$$Q_e(\omega) = \iiint_{V_{NP}} q_e(\omega,r)dV$$

(equation SI 7)

9

and the numerical computation of the absorption cross section σ_abs (ω) is achieved:

$$\sigma_{abs}(\omega) = \frac{Q_e(\omega)}{I_0}$$

(equation SI 8)

I_0 is the illumination intensity (W/m^2).

The power coupling efficiency parameter, denoted as η, can be defined as the ratio of the total power absorbed by the AuNRs deposited on a surface of area A to the total irradiation power incident on the same surface.

$$\eta(\omega) = \frac{Q_{tot}(\omega)}{P_{in}} = \frac{Q_{tot}(\omega)}{I_0 A} = \frac{\frac{Q_e(\omega)\,A}{a}}{I_0 A} = \frac{Q_e(\omega)}{I_0 a} = \frac{\sigma_{abs}(\omega)}{a}$$

(equation SI 9)

The overall surface of area A is considered as composed of elementary portions of area a, characterized by a constant surface density of absorbed power Qe/a, thus:

$$Q_{tot}(\omega) = \frac{Q_e(\omega)}{a}A$$

(equation SI 10)

Figure SI 8a provides numerical results relevant to the absorption spectra of AuNRs deposited on the glass surface: simulations refer to the random distribution of 30 AuNRs on a 0.25 μm^2 glass surface, whose geometrical and EM characteristics have been previously described. **Figure SI 8a** (cyan curve) shows the FEM simulation that uses the AuNRs length deviations distribution

(average length 51 nm, standard deviation, sd= 3 nm) obtained from the experimental morphological analysis (Figures 1 e and 1f and **Figure SI 5**) of the sample: the plot shows the two LSPR- t and LSPR-l absorption peaks, localized at λt= 500 nm and λl=740 nm, respectively, and a full width at half maximum (FWHM) of 90 nm relevant to the main peak.

Figure SI 8a (magenta curve) refers to a second FEM simulation in which AuNRs are modeled as having an equal length (standard deviation sd= 0). Notably, the plot exhibits a FWHM of 55 nm, confirming the relationship between FWHM and the distribution of AuNRs' length deviations. **Figure SI 8a** (black curve) shows the experimental results already demonstrated in **Figure 1a.** The slight difference between the simulation and the experimental details in spectral position and FWHM can be ascribed to the effect of the partial submersion of AuNRs in the PEM layer, as elaborated earlier (refer to **Figures 1 c** and **1d**).

The results obtained from the analytical model, detailed in **Section SI 8**, depicting the macroscopic system's thermal PT response, are presented in **Figure SI 8b** as dashed lines. The plot illustrates the system's mean temperature (T) plotted against irradiation time for various intensities of incident radiation, encompassing an overall simulation period of 300 seconds. PT effects are initiated at the moment t=5s when the NIR laser beam is activated, thereby inducing an electromagnetic response that increases the system's temperature. The heating effect is mitigated by heat dissipation mechanisms, which aim to stabilize the temperature dynamics and achieve an equilibrium temperature within approximately 180 s. Following this period, the laser illumination is deactivated at t=180 s, initiating a cooling process driven by a diminishing thermal gradient, resulting in a gradual decrease in temperature that asymptotically approaches ambient levels. **Figure SI 8b** includes the experimental measurements for reference (straight lines). A comparison between the experimental data and analytical predictions underscores the impact of thermal gradients within the system attributed to the non-uniform illumination of the glass slide surface.[4-6] However, a good agreement

between the theoretical curves and the experimental results for each NIR laser intensity value is worth underlying.
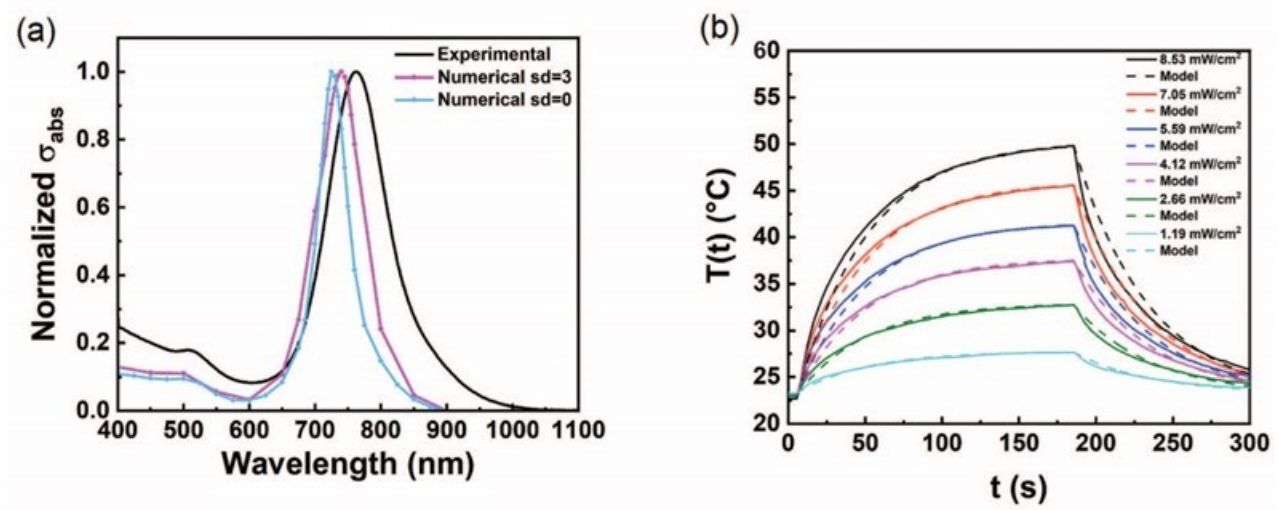

Figure SI 8 Values of the absorption cross-section of the simulated sample are plotted versus the wavelength of incident radiation, showing the transverse plasmon band and LPB occurrence. Absorption peaks localized at λ_t=500 nm and λ_l=740 nm, respectively, and a FWHM of 90 nm (a). Thermal response reported as time-temperature profiles of the macroscopic system resulting from the analytical model (dashed lines) compared with the values obtained from the experimental measurements (straight lines) (b).

SI 8: Thermal response model of the microscopic system- Methods

The laser-irradiated AuNR array is characterized by its mass density ρ= 2500 kg/m³ and geometrical dimensions width, length, and thickness of 1 cm, 1 cm, and 1.1 mm, respectively. The thermal response of the macroscopic system may be analytically modeled by its overall energy balance equation.[3]

$$\sum_i m_i C_{p,i} \frac{dT}{dt} = Q_s + Q_{ext}$$

(equation SI 11)

The left side of Eq. (SI 11) involves masses m_i, specific heat capacity at a constant pressure $C_{p,i}$ of the system components (namely glass slide and AuNRs), the overall system temperature T and time t. The right side of Eq. (SI 11) considers energy exchanges per time unit. The power source term Q_c describes heat flow into the system due to laser irradiation coupling with glass substrate (Q_o) and AuNRs layer (Q_{NP}), thus $Q_c = Q_0 + Q_{NP}$, while power loss Q_{ext} accounts for conductive (Q_{cond}), convective (Q_{conv}), and radiative (Q_{rad}) heat transfer mechanisms, thus $Q_{ext} = Q_{cond} + Q_{conv} + Q_{rad}$.

The radiative transfer term Q_{rad} is approximatively linear for limited temperature increases from the ambient temperature $(T - T_{amb})$ allowing the definition of a proportionality constant γ [W/K] to describe all heat loss terms.[4]

$$Q_{ext} = \gamma(T - T_{amb})$$ (equation SI 12)

The equation governing the thermal response becomes:

$$\sum_i m_i C_{p,i}\frac{dT}{dt} = Q_c + \gamma(T - T_{amb})$$ (equation SI 13)

By normalizing temperatures with respect to the maximum value T_{max}:

$$\theta = \frac{(T_{amb} - T)}{(T_{amb} - T_{max})}$$ (equation SI 14)

and a system time constant τ_s defined as:

$$\tau_s = \frac{\sum_i m_i C_{p,i}}{\gamma}$$ (equation SI 15)

Eq. (SI 8) becomes:

$$\frac{d\theta}{dt} = \frac{1}{\tau_s}\left[\frac{Q_c}{\gamma(T_{max} - T_{amb})} - \theta\right]$$ (equation SI 16)

Which can be addressed in two distinct regimes: forced heating and free cooling.

In the laser heating phase, the maximum temperature T_{max} is reached when thermal equilibrium is achieved:

$$Q_c = Q_{ext} \rightarrow Q_s = \gamma(T_{max} - T_{amb})$$ (equation SI 17)

Eq. (SI 8) becomes:

$$\frac{d\theta}{dt} = \frac{-\theta}{\tau_s}$$ (equation SI 18)

To be solved with the initial condition $T = T_{amb}|_{t=0} \rightarrow \theta = 0|_{t=0}$, yielding

$$\theta = 1 - e^{-\frac{t}{\tau_s}}$$ (equation SI 19)

14

i.e., explicitly,

$$T = T_{amb} - (T_{amb} - T_{max})\left(1 - e^{-\frac{t}{\tau_s}}\right)$$

(equation SI 20)

giving $T|_{t=0} = T_{amb}$ and $T|_{t\to\infty} = T_{max}$.

In the free-cooling phase, the laser irradiation is discontinued, thus, $Q_s = 0$ and Eq. (SI 16) reduces to:

$$\theta = e^{-\frac{t}{\tau_s}}$$

(equation SI 21)

The equation must be solved with the initial condition $T = T_{max}|_{t=0} \to \theta = 1|_{t=0}$, giving:

$$\theta = e^{-\frac{t}{\tau_s}}$$

(equation SI 22)

i.e., explicit :

$$T = T_{amb} - (T_{amb} - T_{max})e^{-\frac{t}{\tau_s}}$$

(equation SI 23)

giving $T|_{t=0} = T_{max}$ and $T|_{t\to\infty} = T_{amb}$.

15

The system time constant τ_s may be determined from experimental data, retrieved in the cooling

$$-\ln\theta = \frac{(t-t_0)}{\tau_s}$$

phase, by plotting values of $\qquad$ and taking the reciprocal of the data linear regression

slope, t_0 is the time instant in which the laser heating is switched off. The results of the analysis are

illustrated in **Figure SI 9.** It turns out in $\tau_s = 57s$. This value accounts for the thermal behavior of

the macroscopic system, which results in being several orders of magnitude slower than the heat

dissipation phenomena at the nanoscale.[5, 7-9] The result is rigorously valid if thermal exchange

dynamics within the system may be neglected.[5, 6]

From Eq. (SI 15), by neglecting heat absorbed by AuNRs, considering only mass and specific heat

capacity of the glass slide:

$$V_g \approx 1cm \cdot 1cm \cdot 1.1mm = 1.1 \cdot 10^{-7}m^3$$,

$$m_g = r_g V_g \approx 2.227 \cdot 10^3 \frac{Kg}{m^3} \cdot 1.1 \cdot 10^{-7}m^3 = 2.45 \cdot 10^{-4}Kg$$

Provided specific heat capacity at constant pressure of glass $C_{p,g} \approx 779.74$ J/ (Kg K), we can

estimate γ, as:

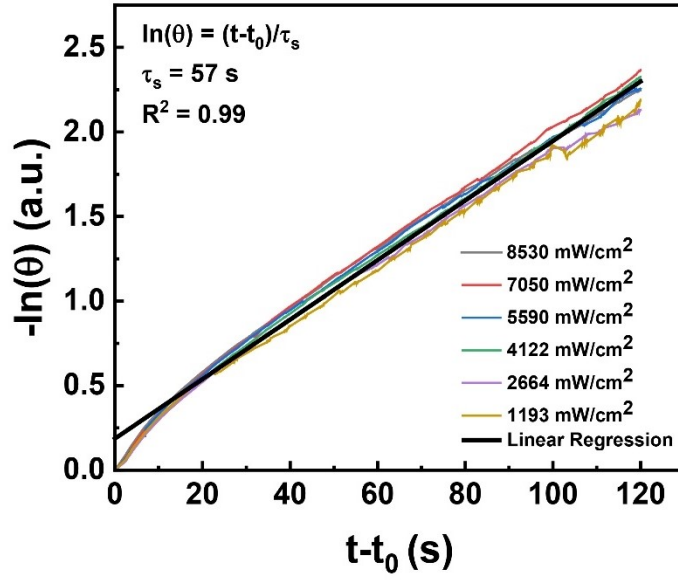$$\gamma = \frac{m_g C_{p,g}}{\tau_s} \approx 3.36 \cdot 10^{-3}$$ W/K   (equation SI 24)

Figure SI 9 Plot of -ln(theta) versus time (t-t₀), t₀ being the initial time of the free cooling. Experimental results are shown for different values of incident laser illumination power. A time constant τ_s =57 s is obtained as the reciprocal of the linear fit slope.

The laser power absorbed by the AuNR array Q_c can be related to incident power Q_{in}:

$$Q_c = \eta Q_{in} \qquad \text{(equation SI 25)}$$

where the parameter η represents a transduction efficiency coefficient.

By neglecting heat dissipated by the non-functionalized glass slide Q_0, from the thermal equilibrium condition in the laser heating phase, we obtain from Eq. (SI 17), by posing $\Delta T_{max} = T_{max} - T_{amb}$ maximum temperature difference after heating:

$$Q_c = \eta Q_{in} = \gamma(T_{max} - T_{amb}) = \gamma \Delta T_{max} \qquad \text{(equation SI 26)}$$

The maximum temperature jump ΔT_{max} may be expressed in terms of the incident power and transduction efficiency η :

$$\Delta T_{max} = \frac{\eta}{\gamma} Q_{in} \quad \text{(equation SI 27)}$$

The values of the ratio $\frac{\eta}{\gamma}$ may be derived from experimental data. Results are reported in **Figure SI 10** in which experimental values of ΔT_{max} are plotted as a function of incident radiation power Q_{in} on the glass substrate.

A value of $\frac{\eta}{\gamma} = 50.8$ is derived from a linear fit of the data. Consequently, the value of power-coupling efficiency parameter $\eta = 0.171$ is obtained from the previously derived value of parameter γ.
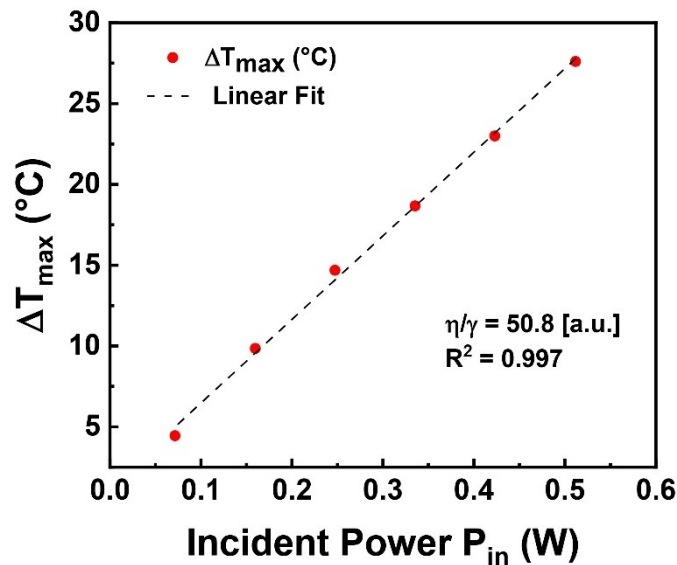

Figure SI 10 Plot of experimental values of the temperature difference at equilibrium ΔT_{max} versus values of laser radiation power Q_{in}, incident on the AuNR array. A value of $\eta/\lambda = 3.0553$ is derived from the slope of linear regression of data.

SI 9: Ability of the cascade AuNR array to perform PT disinfection of bulk water

The PT response of the cascade AuNR array and the cascade AuNR array CG was investigated using the thermo-optical setup (**Figure SI 11a**) realized for PT disinfection experiments.

The first set of PT characterization experiments was carried out without the insulating container shown in **Figure SI 11a**.

In particular, the sample under investigation was placed inside a beaker and irradiated with the NIR laser at power density I=2.32 W/cm^2 for five minutes. Under these experimental conditions, the cascade AuNR array reached a maximum temperature of 76.80°C after 5 min of irradiation (magenta line in **Figure SI 11b**).

When the cascade AuNR array was immersed in the beaker filled with 1.1 mL of tap water (in compliance with the experimental conditions selected for the disinfection experiment), the maximum temperature measured after 5 min of irradiation decreased to 52.4 °C (**Figure SI 11b** cyan line). The same PT characterization carried out in tap water, using the cascade AuNR array CG, produced a PT heating of 52.4°C (**Figure SI 11b**, blue line). However, a more reliable measurement of the PT heating can be obtained by plotting the average temperature values as a function of irradiation time.

The average temperature is supposed to reflect the bulk temperature experienced by bacterial cells in water. The average temperature value (**Figure SI 11c**) measured at the end of the irradiation process was 27.6 °C for the cascade AuNR array in dry conditions (magenta curve). Conversely, when the cascade AuNR array was immersed in water, the average temperature value reached at the end of the experiment was 35.9°C (cyan line in **Figure SI 11c**). Interestingly, when the cascade AuNR array CG was submerged in water under these experimental conditions, it registered a mean temperature of 35.9°C after the irradiation period (as denoted by the blue line in **Figure SI 11**). To summarize, the variation in maximum temperature values is as follows: cascade AuNR array (dry) > cascade AuNRs in tap water = cascade AuNRs CG in tap water. Conversely, the trend for average temperature values is as follows: AuNRs CG in tap water = cascade AuNR array in tap water > cascade AuNR array (dry).
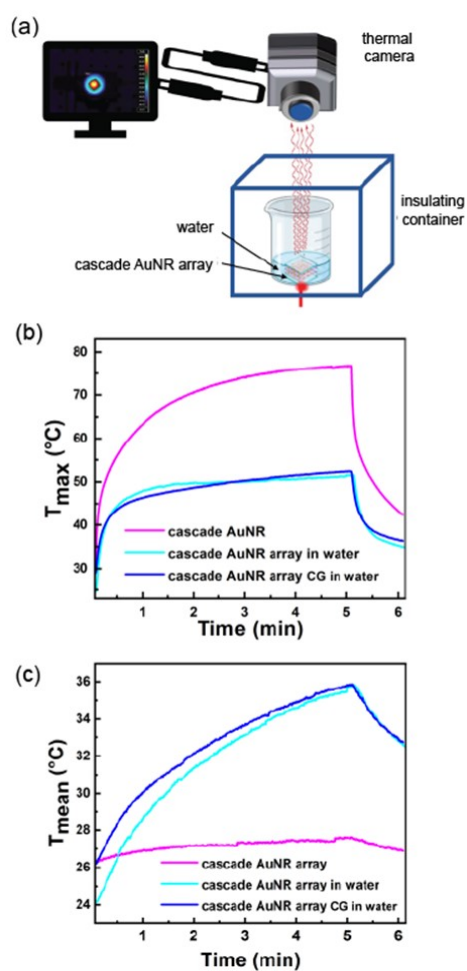
Figure SI 11 Schematic of the thermo-optical setup realized to investigate the PT behaviour of the cascade AuNR array, and the cascade AuNRs array CG in dry conditions and immersed in water (a). Time-temperature profiles report the values of the maximum (b) and mean (c) temperatures.
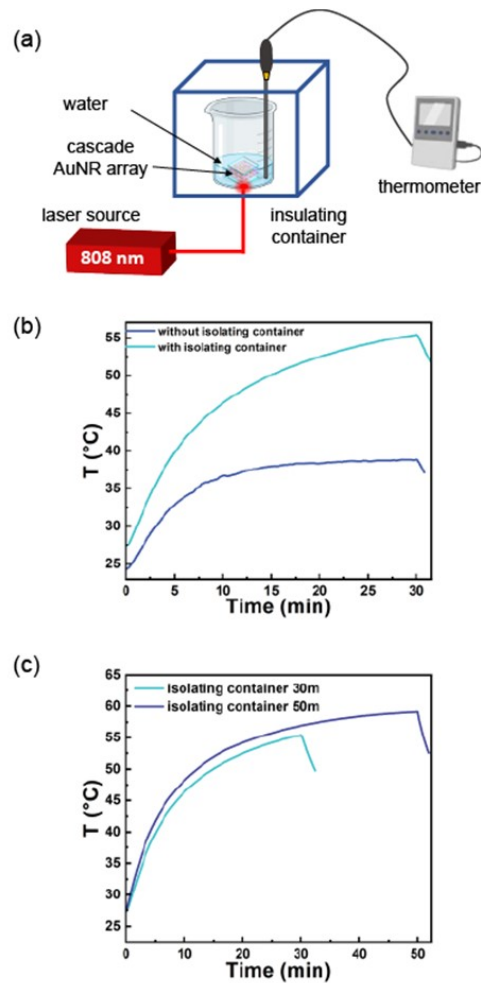
Figure SI 12 Schematic of the thermo-optical setup developed for performing PT disinfection of tap water. (a) Time-temperature profile resulting from the 30 min irradiation of the cascade AuNR array GC immersed in tap water without (turquoise line) and with (blue line) the insulating container. (b) Time-temperature profile resulting from the irradiation of the cascade AuNR array CG immersed in tap water for 30 min (turquoise line) and for 50 min (blue line) with the insulating container (c).

The maximum temperature values are higher than the average values because the average temperature values are mediated within the region of interest (ROI), which includes the entire base surface of the backer that is not effectively heated up by the sample. Noteworthy, considering the cascade AuNR array, the average temperature value, measured before shutting down the laser, was higher when the experiment was performed in tap water (35.9 °C) than in a dry state (27.6 °C). This result accounts for the higher thermal conductivity of water (0.5918 W/m·K at 20°C) to the thermal conductivity of air (0.025 W/m·K at 20°C). Moreover, the average temperature values, measured during the whole NIR laser irradiation time, show that the cascade AuNR array CG exhibited a PT heating greater than the one measured for the cascade AuNR array, contrary to the trend reported in **Figure SI 11b**.

Indeed, focusing on the magenta curve in **Figure SI 11c,** the cascade AuNR array (dry) induced an average heating of 27.6°C. In comparison, the cascade AuNR array CG in water (**Figure SI 11c**, blue curve) promoted a photothermal heating of 35.9 °C. Such a behavior can be associated with the medium's thermal conductivity (as previously elucidated) and with the role played by the n of the surrounding medium.

Therefore, as highlighted in **Figure 3b**, the change in n, occurring upon immersion in tap water, shifted the LPB for the cascade AuNR array CG at a wavelength in resonance with the NIR laser emission wavelength, thus maximizing the PT heating. This evidence supports the faster average temperature increase observed in tap water for the cascade AuNR array CG (**Figure SI 11c**, blue curve) to respect the cascade AuNRs (**Figure SI 11c**, cyan curve).

The thermo-optical setup reported in **Figure SI 11a** was modified to measure the bulk temperature and validate the mean temperature data (**Figure SI 11c**) obtained using the thermo-optical setup in **Figure SI 11a**

In this new configuration (**Figure SI 12a**), the thermal camera was replaced with an immersion digital thermometer. This modification allowed for direct temperature monitoring throughout the irradiation period. Unlike the thermal camera, which calculates an algebraic average of temperatures within the selected ROI, the digital contact thermometer submerged in the water-filled beaker offers a more precise measure of the bulk temperature. This enhancement ensures a more accurate estimation of water temperature.

Based on the results obtained in **Figure SI 11c**, the PT analysis was performed using the cascade AuNR array CG as a thermo-optical transducer. Moreover, to generate a more uniform temperature distribution, we performed the new experiments by irradiating the cascade AuNR array CG, immersed in 1.1 mL of tap water for a longer time (30 min).

Experimental data show that, under these conditions, the average temperature value of 38.8 °C was reached at the end of the irradiation time (blue line in **Figure SI 12b**). Such a result refers to a temperature increase uniformly distributed throughout the volume of water in 30 minutes of illumination, and, remarkably, it is consistent with the data obtained from the analysis of thermographic images (**Figure SI 11c**, blue line).

To further improve the temperature increase, the thermo-optical setup in **Figure SI 12a** was equipped with a thermal isolation box to prevent heat dissipation, thus increasing the highest

temperature value. This improvement in the experimental setup allowed the temperature to rise to 55.4 °C after 30 minutes of illumination (turquoise line in **Figure SI 12b**) but without reaching a plateau. Instead, by increasing the irradiation time to 50 min, the heat photogenerated by the cascade AuNR array CG raised the water temperature to 59.1 °C (**Figure SI 12c**, blue line). As this value is expected to induce bacteria inactivation, these experimental conditions were used for performing PT disinfection experiments.

References

1. Cottat, M.; Thioune, N.; Gabudean, A.-M.; Lidgi-Guigui, N.; Focsan, M.; Astilean, S.; Lamy de la Chapelle, M., Localized surface plasmon resonance (LSPR) biosensor for the protein detection. *Plasmonics* **2013,** *8*, 699-704.

2. Petronella, F.; De Biase, D.; Zaccagnini, F.; Verrina, V.; Lim, S. I.; Jeong, K. U.; Miglietta, S.; Petrozza, V.; Scognamiglio, V.; Godman, N. P.; Evans, D. R.; McConney, M.; De Sio, L., Label-free and reusable antibody-functionalized gold nanorod arrays for the rapid detection of Escherichia coli cells in a water dispersion. *Environ. Sci. Nano* **2022,** *9* (9), 3343-3360.

3 B. Johnson and R.-W. Christy, Optical constants of the noble metals, *Physical review B*, 1972, **6**, 4370.

4 Roper, D. K.; Ahn, W.; Hoepfner, M., Microscale heat transfer transduced by surface plasmon resonant gold nanoparticles. *The Journal of Physical Chemistry C* **2007,** *111* (9), 3636-3641.

5 Evans, P. G., Surface Plasmon Enhanced Heating of Gold Nanoparticles: A Plasmonic Optical Switch. **2007**.

6 W. Jo, K. Freedman, D. K. Yi, R. K. Bose, K. K. Lau, S. D. Solomon and M. J. Kim, Photon to thermal response of a single patterned gold nanorod cluster under near-infrared laser irradiation, Biofabrication, 2011, 3, 015002

7. Hatef, A.; Fortin-Deschênes, S.; Boulais, E.; Lesage, F.; Meunier, M., Photothermal response of hollow gold nanoshell to laser irradiation: Continuous wave, short and ultrashort pulse. *International Journal of Heat and Mass Transfer* **2015,** *89*, 866-871.

8. Ekici, O.; Harrison, R.; Durr, N.; Eversole, D.; Lee, M.; Ben-Yakar, A., Thermal analysis of gold nanorods heated with femtosecond laser pulses. *Journal of physics D: Applied physics* **2008,** *41* (18), 185501.

9. Gan, R.; Fan, H.; Wei, Z.; Liu, H.; Lan, S.; Dai, Q., Photothermal response of hollow gold nanorods under femtosecond laser irradiation. *Nanomaterials* **2019,** *9* (5), 711.